JEM Journal of Experimental Medicine

BRIEF DEFINITIVE REPORT

RNase T2 restricts TLR13-mediated autoinflammation in vivo

Carlos Gomez-Diaz[1], Wilhelm Greulich[1], Benedikt Wefers[2,3,4,5], Meiyue Wang[1], Silvia Bolsega[6], Maike Effern[7], Daniel P. Varga[8], Zhe Han[9], Minyi Chen[9], Marleen Bérouti[1], Natascia Leonardi[1], Ulrike Schillinger[1], Bernhard Holzmann[10], Arthur Liesz[5,8], Axel Roers[9], Michael Hölzel[7], Marijana Basic[6], Wolfgang Wurst[2,3,4], and Veit Hornung[1]

RNA-sensing TLRs are strategically positioned in the endolysosome to detect incoming nonself RNA. RNase T2 plays a critical role in processing long, structured RNA into short oligoribonucleotides that engage TLR7 or TLR8. In addition to its positive regulatory role, RNase T2 also restricts RNA recognition through unknown mechanisms, as patients deficient in RNase T2 suffer from neuroinflammation. Consistent with this, mice lacking RNase T2 exhibit interferon-dependent neuroinflammation, impaired hematopoiesis, and splenomegaly. However, the mechanism by which RNase T2 deficiency unleashes inflammation in vivo remains unknown. Here, we report that the inflammatory phenotype found in *Rnaset2*$^{-/-}$ mice is completely reversed in the absence of TLR13, suggesting aberrant accumulation of an RNA ligand for this receptor. Interestingly, this TLR13-driven inflammatory phenotype is also fully present in germ-free mice, suggesting a role for RNase T2 in limiting erroneous TLR13 activation by an as yet unidentified endogenous ligand. These results establish TLR13 as a potential self-sensor that is kept in check by RNase T2.

Introduction

The host employs pathogen recognition receptors (PRRs) to detect pathogen-associated molecular patterns (PAMPs) as nonself. TLRs are a family of PRRs sensing different conserved microbial features (Fitzgerald and Kagan, 2020). They allow for the recognition of a wide variety of microbes and viruses, leading to innate and adaptive immune responses (Lind et al., 2022). Five mammalian TLRs sense the presence of microbial nucleic acids (TLR3, TLR7, TLR8, TLR9, and TLR13). TLR3 senses double-stranded RNA. TLR7 and TLR8 detect RNA degradation products while TLR9 senses single-stranded DNA containing unmethylated CpG motifs (Lind et al., 2022). Absent in humans, TLR13 is expressed in rodents and detects single-stranded RNA (ssRNA) from bacterial sources in a sequence-specific manner (Li and Chen, 2012; Oldenburg et al., 2012; Song et al., 2015). To avoid activation by endogenous nucleic acids, nucleic acid–sensing TLRs reside in the endolysosome with the ligand-binding domains facing the lumen of the compartment. The abundance of endogenous nucleic acids is regulated by the function of nucleases, and the sensitivity of TLR receptors is modulated by additional licensing signals such as type I IFN. Inside the endolysosome, the endoribonuclease RNase T2 processes long-structured ssRNA to make it detectable to human TLR8 and TLR7 (Berouti et al., 2024; Greulich et al., 2019; Ostendorf et al., 2020). TLR8 consists of homodimers arranged in a rotational symmetry where the leucine-rich repeat ligand-binding domains face the lumen of the endolysosome. Structural studies have described two ligand-binding pockets that engage different RNA molecules (Tanji et al., 2015). Uridine binds to the first binding pocket of TLR8, while the 2′,3′-cyclophosphate–terminated fragments can engage the second binding pocket of TLR8 (Greulich et al., 2019; Tanji et al., 2015). RNase T2 cleaves ssRNA between purine and uridine residues, contributing to increasing the pool of catabolic uridine and the generation of adenosine or guanosine 2′,3′-cyclophosphate–terminated fragments (Greulich et al., 2019; Ostendorf et al., 2020). In humans, RNase T2 deficiency is the cause for a rare, monogenetic, early childhood onset cystic leukoencephalopathy characterized by neurological deficits and brain magnetic resonance imaging findings of cystic lesions, white matter changes, and cerebral atrophy (Henneke et al., 2009). RNase T2 deficiency has been

[1]Gene Center and Department of Biochemistry, Ludwig-Maximilians-Universität München, Munich, Germany; [2]Institute of Developmental Genetics, Helmholtz Zentrum München, Neuherberg, Germany; [3]TUM School of Life Sciences, Technische Universität München, Freising-Weihenstephan, Germany; [4]Deutsches Zentrum für Neurodegenerative Erkrankungen Site Munich, Munich, Germany; [5]Munich Cluster for Systems Neurology (SyNergy), Munich, Germany; [6]Institute for Laboratory Animal Science, Hannover Medical School, Hannover, Germany; [7]Institute of Experimental Oncology, Medical Faculty, University Hospital Bonn, Bonn, Germany; [8]Institute for Stroke and Dementia Research, University Hospital, Ludwig-Maximilians-Universität München, Munich, Germany; [9]Institute for Immunology, Heidelberg University Hospital, Heidelberg, Germany; [10]Department of Surgery, TUM School of Medicine and Health, Technical University of Munich, Munich, Germany.

Correspondence to Veit Hornung: hornung@genzentrum.lmu.de.

suggested to be a type I interferonopathy, a disease spectrum characterized by mutations in nucleic acid sensing or metabolism pathways that cause inappropriate or excessive type I IFN production, leading to chronic inflammation and autoimmune symptoms (Crow and Stetson, 2022). However, unlike classic interferonopathies, the type I IFN signature in RNase T2–deficient patients is rather subtle (Rice et al., 2017). In mice, RNase T2 deficiency results in an increased type I IFN signature in various tissues, as well as splenomegaly and dysregulated hematopoiesis (Kettwig et al., 2021). Therefore, it is conceivable to propose that RNase T2 limits the pool of RNAs in the lysosome, therefore restricting spurious activation of RNA sensors.

Here, we set out to study the role of RNase T2 in regulating inflammation in mice in vivo. We show that *Rnaset2*$^{-/-}$ mice suffer from an inflammatory phenotype characterized by an enlarged spleen displaying a dysregulated immune cell composition with increased myeloid cells and peripheral leukocytosis. We delineate a TLR13-myeloid differentiation primary response 88 (MyD88)–dependent signaling cascade instigating inflammation in the absence of RNase T2. Surprisingly, we found that the inflammatory phenotype of *Rnaset2*$^{-/-}$ mice is independent of the microbiome. As such, we propose that RNase T2 deficiency leads to the endolysosomal accumulation of a yet undefined endogenous RNA molecule activating TLR13-mediated inflammation.

Results and discussion

RNase T2 deficiency results in hepatosplenomegaly, leukocytosis, and anemia

Mice possess two paralogs of RNase T2—*Rnaset2a* and *Rnaset2b*—which are located in close proximity on chromosome 17. Despite minor differences at the DNA sequence level, the protein products of these genes are identical. To generate RNase T2–deficient mice, we used a CRISPR-Cas9 approach to target both loci simultaneously, deleting exons 2–4 of each gene. Mice carrying deletions in both *Rnaset2a* and *Rnaset2b* were identified by genotyping and subsequently bred to homozygosity. In the following, these mice will be referred to as *Rnaset2*$^{-/-}$ mice. Consistent with previous reports, RNase T2–deficient mice were born at Mendelian ratios yet developed splenomegaly as early as 8 wk of age (Fig. 1, A–C) (Kettwig et al., 2021). Characterization of the immune cell composition in the spleens of 8–12-wk-old mice revealed an increased proportion of the myeloid compartment (CD11b$^+$ cells) (Fig. 1 D), which included elevated levels of neutrophils and CD11b$^+$ dendritic cells (Fig. S1 A and Table S1). Notably, we also observed a significant increase in CD11b$^+$ B cells, a phenotype associated with age-associated B cells (ABCs) implicated in autoimmunity (Mouat et al., 2022), as well as a rise in F4/80$^+$ macrophages. In contrast, the proportions of T cells and CD19$^+$ B cells were relatively decreased (Table S1). Aged mice (40–54 wk old) showed similar features of splenomegaly and increased myeloid cell proportions with an even more pronounced increase in the aforementioned cell populations (Fig. 1, E–H and Table S1). Associated with this splenomegaly, analysis of peripheral blood from aged *Rnaset2*$^{-/-}$ revealed a drastic leukocytosis that is characterized by both lymphocytosis and neutrophilia, as well as signs of regenerative anemia as evidenced by a reduced RBC count and concomitant reticulocytosis (Fig. 1 I). Further, *Rnaset2*$^{-/-}$ displayed a marked thrombocytopenia as evidenced by a low platelet count in the peripheral blood (Fig. 1 I). To explore whether the observed changes in the peripheral blood stem from a possible defect in myelopoiesis in *Rnaset2*$^{-/-}$ mice, we collected bone marrow samples and subjected them to CFU assays to evaluate the ability of the hematopoietic progenitor cells to form colonies. However, these assays did not show any overt differences between *Rnaset2*$^{+/+}$ and *Rnaset2*$^{-/-}$ mice (Fig. 1 J). In contrast, we observed a marked increase in hemophagocytosis within splenic macrophages in RNase T2-deficient mice. Specifically, when staining intracellularly for the erythroid marker Ter-119, CD169-negative macrophages—indicative of red pulp macrophages (RP macrophages)—exhibited a pronounced increase in Ter-119 signal (Fig. 1, K and L). Given the increase in ABCs, we also examined whether RNase T2-deficient mice would develop autoantibodies. Indeed, the absence of RNase T2 promoted the production of autoantibodies against ubiquitous nuclear antigens (antinuclear antibodies [ANAs], Fig. 1, M and N). While the spontaneous development of low-level ANAs in a subset of aged WT C57BL/6 mice is a known phenomenon (Nusser et al., 2014), we observed a notable increase in ANA incidence and titers in aged *Rnaset2*$^{-/-}$ mice. Furthermore, analysis of serum from aged RNase T2–deficient mice, in comparison to WT mice, revealed significantly elevated levels of the pro-inflammatory cytokines CXCL1, IL-12p70, and IL-6, along with a moderate increase in the antiviral factor IP-10 and higher IL-10 levels (Fig. S1 B). Altogether, these results suggest that RNase T2 deficiency leads to a mixed autoinflammatory and autoimmune syndrome characterized by splenomegaly, leukocytosis, increased pro-inflammatory mediators, and autoantibody formation. Additionally, these mice develop anemia and thrombocytopenia, which could be secondary to the observed splenomegaly or a direct result of the observed dysregulated hemophagocytosis.

RNase T2 deficiency–associated inflammation depends on MyD88 signaling

To define the immune signaling cascade instigating inflammation in RNase T2–deficient mice, we knocked out the key signaling adaptor proteins MyD88 and TIR-domain-containing adapter-inducing INF-β (TRIF) (gene name *Ticam1*). MyD88 is common to all TLRs, while TRIF acts as a signaling adaptor required for TLR3 and TLR4 signaling (Yamamoto et al., 2002, 2003). Furthermore, the role of the cGAS-STING DNA-sensing pathway in instigating inflammation in RNase T2–deficient mice was also evaluated by deleting the signaling effector STING. The macroscopic splenomegaly in RNase T2–deficient mice was completely ameliorated in *Rnaset2*$^{-/-}$*; Myd88*$^{-/-}$ mice, whereas genetic deletion of TRIF in an RNase T2–deficient background did not rescue these phenotypes (Fig. 2 A). *Rnaset2*$^{-/-}$*; Sting*$^{-/-}$ mice, on the other hand, showed an intermediate phenotype, suggesting a partial or secondary contribution of the STING pathway. Quantifying spleen size and myeloid cell expansion supported these observations in young (Fig. 2, B and C) and in aged mice (Fig. 2, D and E). Immunofluorescence studies of the

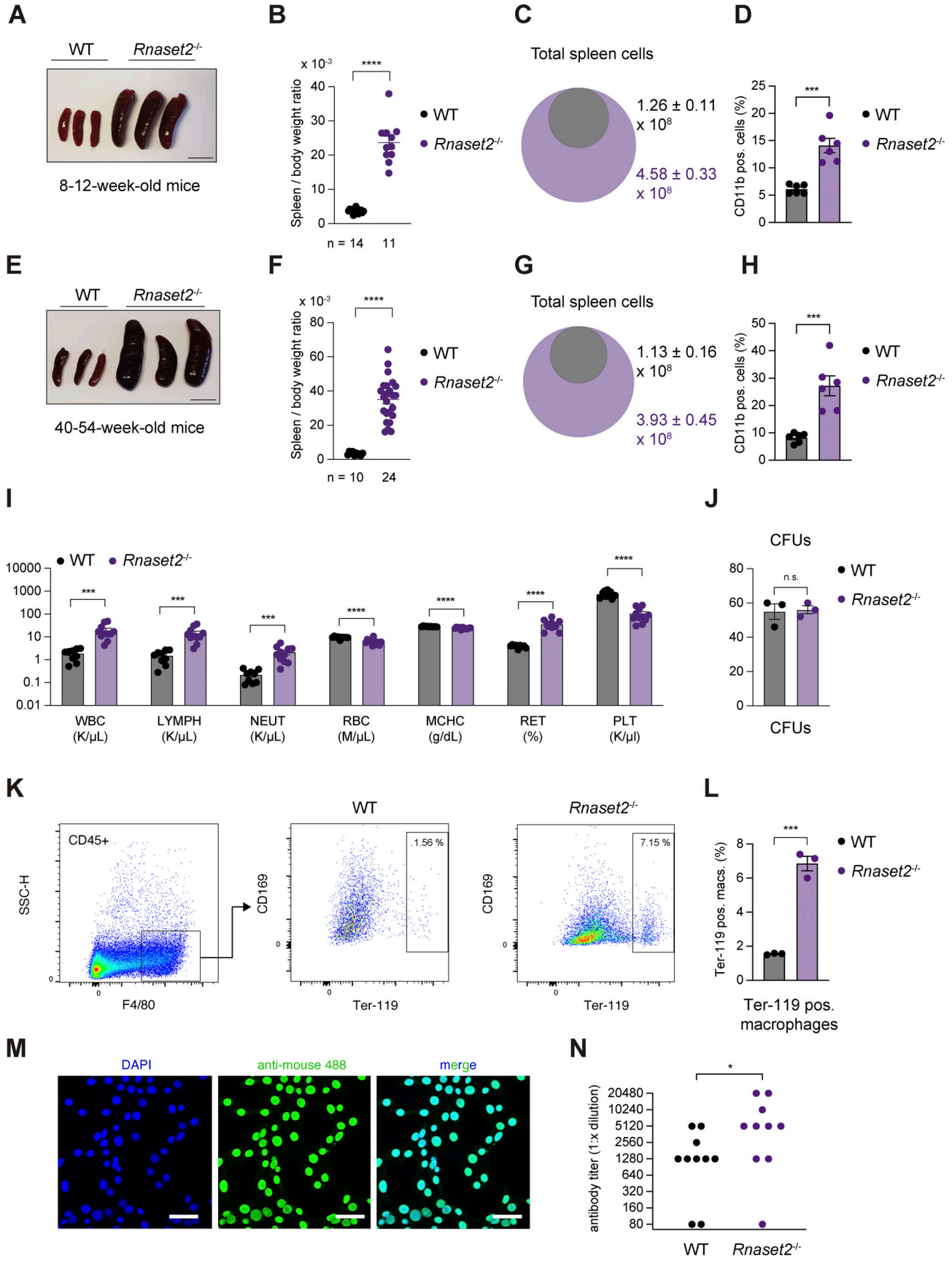

Figure 1. ***Rnaset2*$^{-/-}$ mice display an autoinflammatory phenotype. (A)** Macroscopic appearance of spleens from young mice of the indicated genotypes, showing images from three representative mice. Scale bar equals 1 cm. **(B)** Spleen-to-body weight ratio in mice of the indicated genotypes. Data are presented

as mean ± SEM, with statistical analysis conducted on all available genotypes using a one-way ANOVA with Dunnett's correction. **(C)** Total spleen cell counts (mean ± SEM) for WT (n = 8) and *Rnaset2*$^{-/-}$ (n = 6) mice. **(D)** Percentages of CD45$^+$ CD11b$^+$ cells (mean ± SEM) in the spleens of young mice of WT (n = 6) and *Rnaset2*$^{-/-}$ (n = 6); statistical analysis performed using an unpaired two-tailed t test. **(E)** Spleen images as shown in A, with three representative mice depicted. **(F)** Spleen-to-body weight ratio for mice of the indicated genotypes (mean ± SEM); statistical analysis performed on all available genotypes using a one-way ANOVA with Dunnett's correction. **(G)** Total spleen cell counts (mean ± SEM) for WT (n = 7) and *Rnaset2*$^{-/-}$ (n = 10) mice. **(H)** Percentages of CD45$^+$ CD11b$^+$ cells (mean ± SEM) in the spleens of aged mice of WT (n = 6) and *Rnaset2*$^{-/-}$ (n = 6); statistical analysis performed using an unpaired two-tailed t test. **(I)** Blood parameters for 40–54-wk-old mice of the indicated genotypes (WT n = 9, *Rnaset2*$^{-/-}$ n = 11), presented as mean ± SEM; statistical analysis performed on all available genotypes using a one-way ANOVA with Dunnett's correction. **(J)** Frequency of hematopoietic progenitor cells in the bone marrow of mice of the indicated genotypes. Data are shown as mean ± SEM for three mice; statistical analysis by using an unpaired two-tailed t test. **(K)** Representative flow cytometry plots showing CD45$^+$ F4/80$^+$ cells from young mice of the indicated genotypes, intracellularly stained for Ter-119. **(L)** Summary of data obtained for mice analyzed as in K for three mice per genotype, presented as mean ± SEM; statistical analysis using an unpaired two-tailed t test. **(M and N)** ANA screening by immunofluorescence analysis of sera from aged WT and *Rnaset2*$^{-/-}$ mice, conducted on murine fibroblasts; representative images (M) of one *Rnaset2*$^{-/-}$ mouse are shown (scale bar = 50 µm). Antibody titers (N) determined by serial dilutions for WT (n = 10) and *Rnaset2*$^{-/-}$ (n = 10) mice. Statistical analysis by Mann–Whitney's U test. Significance levels are indicated as *P < 0.05, ***P < 0.001, and ****P < 0.0001; n.s. = not significant.

spleen tissue confirmed the increased abundance of myeloid cells (CD11b$^+$ cells) in the spleen of *Rnaset2*$^{-/-}$ mice (Fig. 2, F and G). Additionally, these analyses demonstrated that the spleens of *Rnaset2*$^{-/-}$ mice exhibited a disruption in their follicular structure, accompanied by an expansion of the RP area at the expense of the marginal zone and the white pulp area (Fig. S2, A and B). This was also associated with a decrease in marginal zone macrophages (CD169$^+$) and an increase in RP macrophages. Of note, all of these changes were completely reverted by additionally ablating MyD88 (Fig. 2, F and G). Altogether, these results indicate that MyD88 is crucial for inflammation and spleen pathology in RNase T2–deficient mice, while the STING pathway may play a secondary role.

Tlr13 is required to instigate inflammation in the absence of RNase T2

We considered two scenarios for the MyD88 dependence of splenomegaly. On one hand, it seemed conceivable that MyD88 transmits a signal downstream of IL-1 family receptors, which could be engaged by IL-1α/β or IL-18 in the context of spontaneous inflammasome activation. At the same time, we considered the possibility that yet another endolysosomal TLR, namely TLR13, is triggering this inflammatory response. TLR13 recognizes endolysosomal ssRNA in a sequence-specific manner (Li and Chen, 2012; Oldenburg et al., 2012; Song et al., 2015), and, unlike TLR7 and TLR8, there is no evidence that a specific upstream processing event is required to regulate ligand availability. Indeed, stimulation of bone marrow–derived macrophages (BMDMs) from RNase T2–deficient mice showed that RNA-dependent TLR7 activation was diminished, whereas the pro-inflammatory activity of a TLR13-stimulatory oligoribonucleotide remained unaffected (Fig. S2, C and D). To explore whether inflammasome or TLR13-mediated signaling instigates inflammation in RNase T2–deficient mice, we generated *Rnaset2*$^{-/-}$; *Pycard*$^{-/-}$ mice, in which the common inflammasome adaptor molecule ASC (apoptosis-associated speck-like protein containing a CARD; gene name *Pycard*) is ablated, as well as *Rnaset2*$^{-/-}$; *Tlr13*$^{-/-}$ mice. Genetic deletion of ASC had no effect on the enlarged spleen and increased number of myeloid cells displayed by RNase T2–deficient mice (Fig. 3, A–E), whereas ablation of TLR13 resulted in a complete reduction of splenomegaly and increased number of myeloid cells in the spleen of both young and aged mice (Fig. 3, A–E). Consistent with a TLR13-MyD88–signaling pathway instigating inflammation, the levels of the pro-inflammatory cytokines IL-12 and IL-6, as well as IL-10, were significantly reduced in the serum of *Rnaset2*$^{-/-}$; *Myd88*$^{-/-}$ and *Rnaset2*$^{-/-}$; *Tlr13*$^{-/-}$ mice (Fig. 3 F). Furthermore, analysis of the blood from *Rnaset2*$^{-/-}$; *Tlr13*$^{-/-}$ and *Rnaset2*$^{-/-}$; *Myd88*$^{-/-}$ mice showed that the leukocytosis, neutrophilia, reticulocytosis, and anemia were also significantly reduced (Fig. 3 G). Collectively, these results delineate a TLR13-MyD88–dependent signaling axis that drives inflammation in the absence of RNase T2, a finding that has also been recently reported by Sato and coworkers (Sato et al., 2025).

The RNase T2 deficiency–associated inflammatory phenotype is microbiome independent

Histological analysis of the brains of both young and aged *Rnaset2*$^{-/-}$ mice revealed neuroinflammation as evidenced by an increased number of microglial (Iba1$^+$) clusters compared with WT controls (Fig. S3, A–F). Given our delineation of a TLR13-MyD88–dependent signaling axis promoting inflammation in *Rnaset2*$^{-/-}$ mice, we investigated whether this axis was responsible for the observed neuroinflammation. Indeed, both young and aged *Rnaset2*$^{-/-}$; *Myd88*$^{-/-}$ and *Rnaset2*$^{-/-}$; *Tlr13*$^{-/-}$ mice showed reduced levels of Iba1$^+$ clusters, suggesting a reduction in neuroinflammation (Fig. S3, A–F). Additionally, we observed a decrease in the percentage of NeuN-positive neurons in the gliotic regions compared with homotypic non-gliotic areas in the *Rnaset2*$^{-/-}$ mice (Fig. S3 G), suggesting that neuroinflammation may lead to neurodegeneration. Similar to neuroinflammation, loss of NeuN-positive neurons was ameliorated in *Rnaset2*$^{-/-}$; *Myd88*$^{-/-}$ and *Rnaset2*$^{-/-}$; *Tlr13*$^{-/-}$ mice (Fig. S3 G). These results implicate the TLR13-MyD88–signaling cascade in the neuroinflammation observed in the absence of RNase T2. Given that the blood–brain barrier serves as a barrier to microorganisms, we speculated that the origin of the RNA accumulated in RNase T2–deficient mice, which drives TLR13-dependent inflammation, is endogenous. As such, we rederived *Rnaset2*$^{-/-}$ mice under germ-free conditions to explore whether germ-free *Rnaset2*$^{-/-}$ mice would develop signs of inflammation. Intriguingly, 8-wk-old germ-free *Rnaset2*$^{-/-}$ mice exhibited hepatosplenomegaly (Fig. 4, A and B; and Fig. S3, H and I). Accordingly, the total number of CD11b+ cells in the spleens of *Rnaset2*$^{-/-}$ mice was significantly increased (Fig. 4 C). Further analysis of the myeloid compartment revealed elevated proportion of ABCs

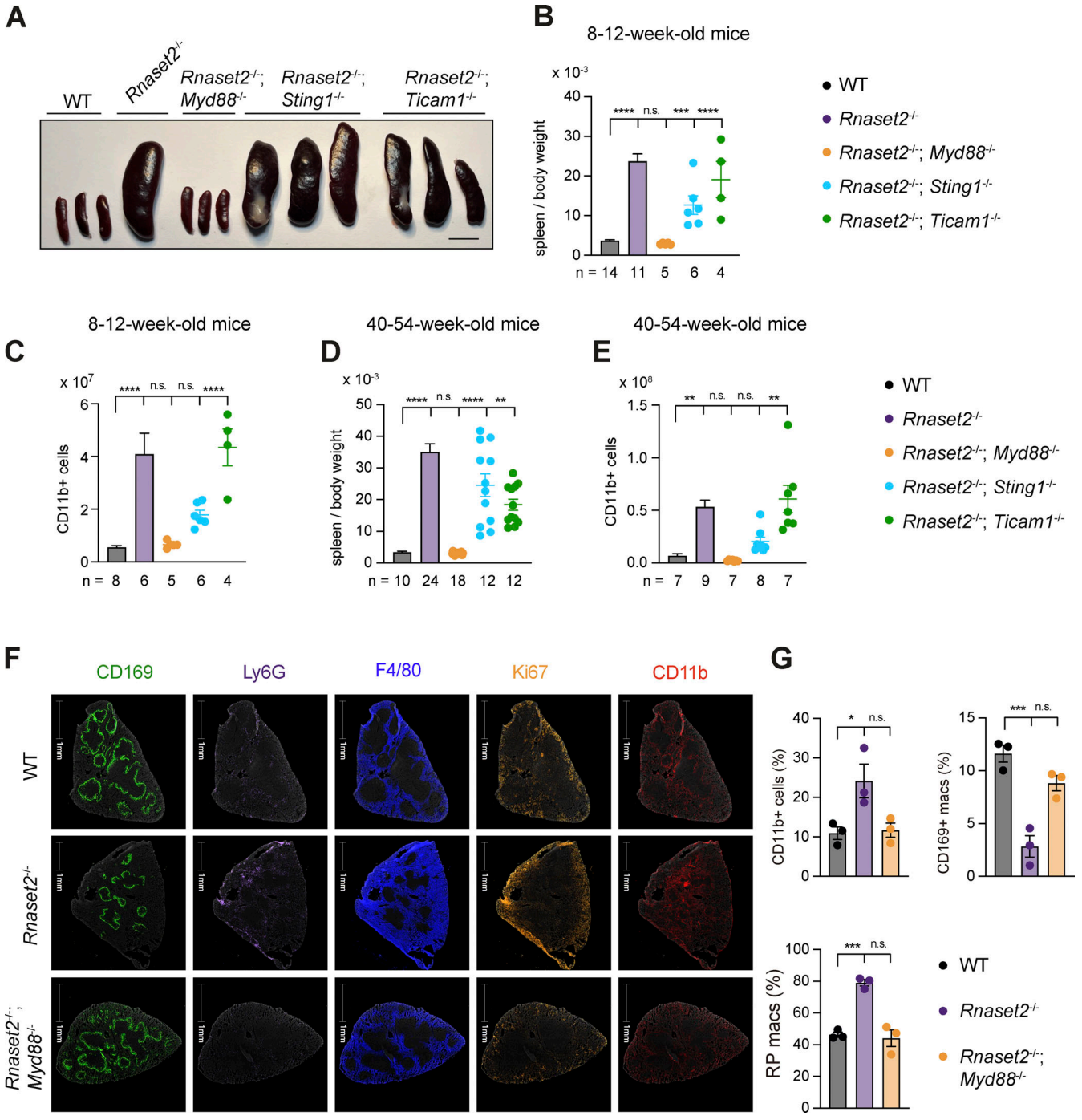

Figure 2. **The pro-inflammatory phenotype in *Rnaset2*$^{-/-}$ mice depends on MyD88. (A)** Macroscopic appearance of spleen of 40–54-wk-old mice from the indicated genotypes. Images of one or three exemplary mice are shown. Scale bar equals 1 cm. **(B)** Spleen-to-body weight ratio of mice of the indicated genotypes. Data are depicted as mean values ± SEM; statistics were calculated on all available genotypes using a one-way ANOVA with a Dunnett correction. For this and the following comparisons, note that when a comparison bar is used to illustrate multiple comparisons, the extended line on the bar indicates the reference data set to which the significance level information applies. **(C)** Total number of CD11b$^+$ cells in the spleens of young mice from the indicated genotypes. Data are depicted as mean values ± SEM; statistics were calculated on all available genotypes using a one-way ANOVA with a Dunnett correction. **(D and E)** Spleen-to-body weight ratio of aged mice and total number of CD11b$^+$ cells in the spleens are presented as in B and C. **(F)** Representative images of CD169, Ly6G, F4/80, Ki67, and CD11b staining from the spleen of 13-wk-old mice of the indicated genotypes. Scale bars equal 1 mm. **(G)** Percentage of CD11b$^+$ cells, CD169$^+$ macrophages and RP macrophages detected in the spleen of mice from the indicated genotypes (n = 3). Data are depicted as mean values ± SEM; statistics were calculated on all available genotypes using a one-way ANOVA with a Dunnett correction. Note that data from the same WT and *Rnaset2*$^{-/-}$ mice, as in Fig. 1, are depicted for B and D. Significance levels are indicated as *P < 0.05, **P < 0.01, ***P < 0.001, and ****P < 0.0001; n.s. = not significant.

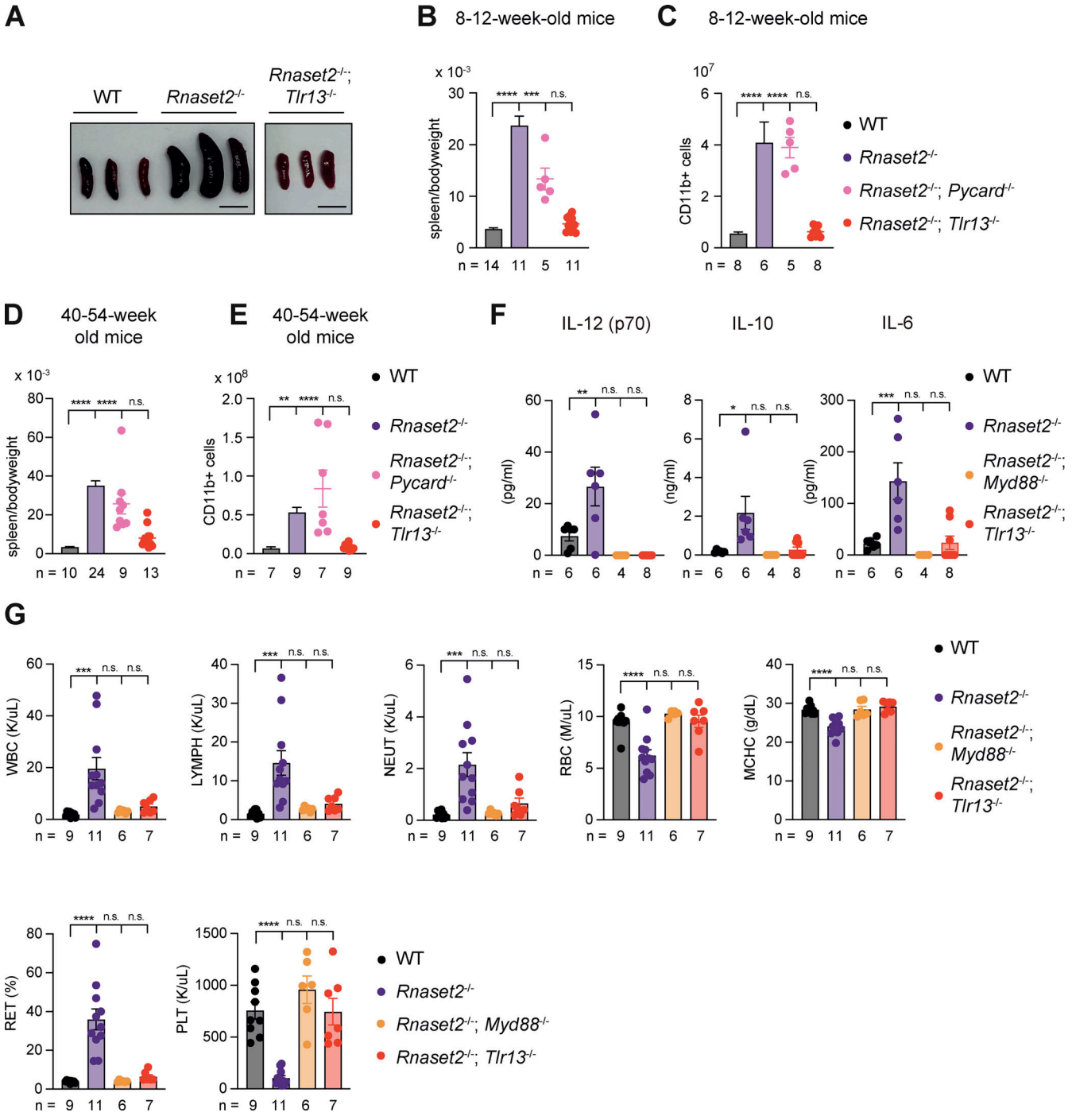

Figure 3. **A MyD88-TLR13–mediated signaling cascade instigates inflammation in *Rnaset2*$^{-/-}$ mice. (A)** Macroscopic appearance of spleen from 8–12-wk-old mice of the indicated genotypes. Scale bar equals 1 cm. **(B)** Spleen-to-body weight ratio of young mice of the indicated genotypes. Data are depicted as mean values ± SEM; statistics were calculated on all available genotypes using a one-way ANOVA with a Dunnett correction. **(C)** Total number of CD11b$^+$ cells in the spleens of young mice from the indicated genotypes. Data are depicted as mean values ± SEM; statistics were calculated on all available genotypes using a one-way ANOVA with a Dunnett correction. **(D and E)** Spleen-to-body weight ratio of aged mice and total number of CD11b$^+$ cells in the spleens are presented as in B and C. **(F)** Serum cytokine levels from 40–54-wk-old mice of the indicated genotypes. Data are depicted as mean values ± SEM; statistics were calculated on all available genotypes using a one-way ANOVA with a Dunnett correction. **(G)** Blood parameters of 40–54-wk-old mice from the indicated genotypes. Data are depicted as mean values ± SEM; statistics were calculated on all available genotypes using a one-way ANOVA with a Dunnett correction. Note that data from the same WT and *Rnaset2*$^{-/-}$ mice, as in Fig. 1, are depicted for B, D, and G, as in Fig. 2 for C and E, and as in Fig. S1 for F. Significance levels are indicated as *P < 0.05, **P < 0.01, ***P < 0.001, and ****P < 0.0001; n.s. = not significant.

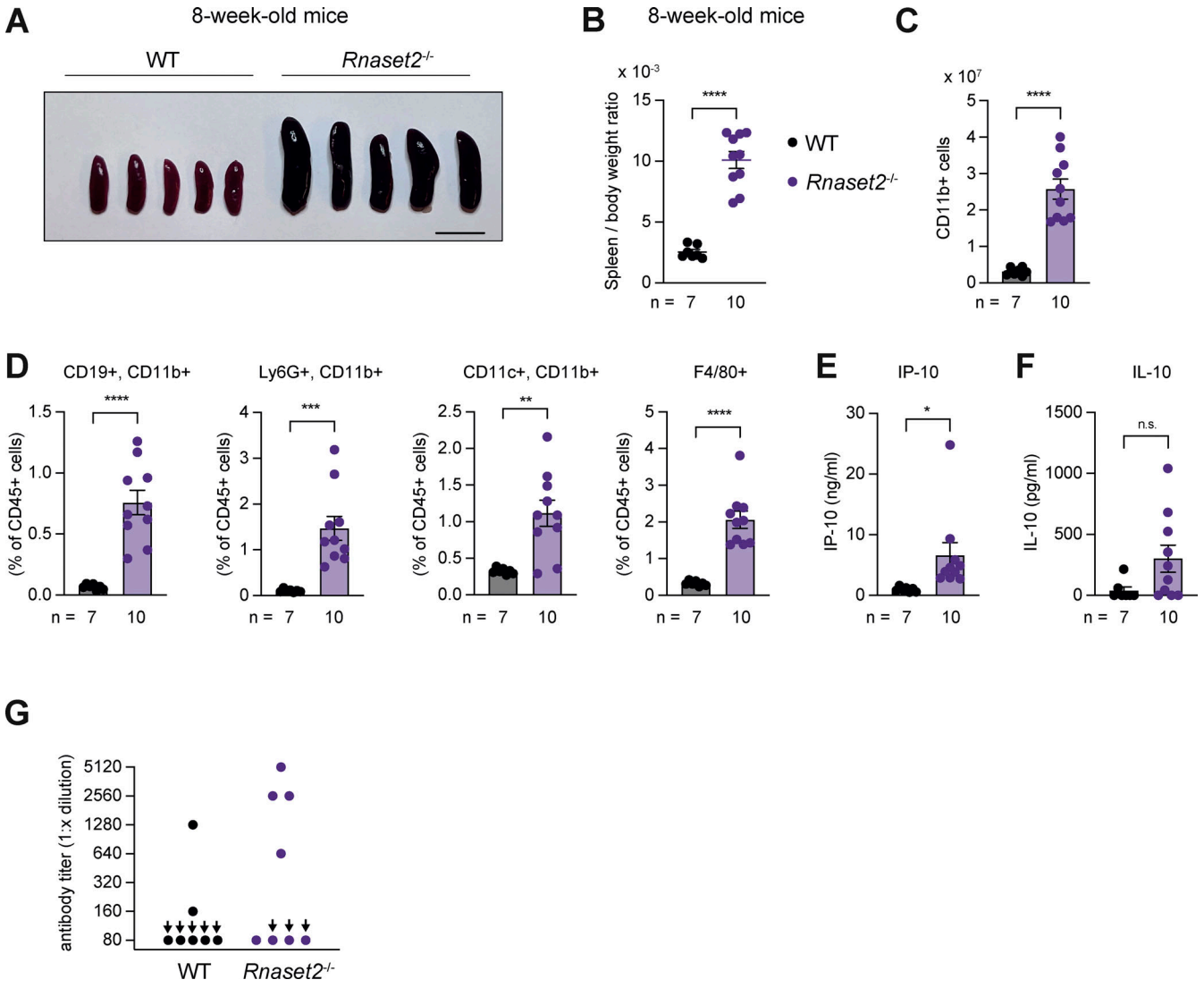

Figure 4. **The pro-inflammatory phenotype presented by *Rnaset2*$^{-/-}$ mice is independent of the microbiome. (A)** Macroscopic appearance of spleens from germ-free, 8-wk-old mice of the indicated genotypes, with images of five representative mice shown. Scale bar equals 1 cm. **(B)** Spleen-to-body weight ratio of 8-wk-old germ-free mice of the indicated genotypes. Data are presented as mean ± SEM; statistical analysis was conducted using an unpaired two-tailed *t* test. **(C)** Total number of CD11b+ cells in the spleens of 8-wk-old germ-free mice of the indicated genotypes. Data are presented as mean ± SEM; statistical analysis was conducted using an unpaired two-tailed *t* test. **(D)** Percentages of CD19$^+$ CD11b$^+$, Ly6G$^+$ CD11b$^+$, CD11c$^+$ CD11b$^+$, and F4/80$^+$ cells in the spleens of young germ-free mice, shown as mean ± SEM; statistical analysis was conducted using an unpaired two-tailed *t* test. **(E and F)** Serum cytokine levels from germ-free, 8-wk-old mice of the indicated genotypes. Data are presented as mean ± SEM; statistical analysis was conducted using an unpaired two-tailed *t* test. **(G)** Autoantibody titers determined by serial dilutions for WT (n = 7) and *Rnaset2*$^{-/-}$ (n = 8) young germ-free mice. The arrow pointing down indicates samples where the measured antibody titer was below 1:80. Significance levels are indicated as *P < 0.05, **P < 0.01, ***P < 0.001, and ****P < 0.0001; n.s. = not significant.

(CD19$^+$ CD11b$^+$), neutrophils (CD11b$^+$ Ly6G$^+$), CD11b$^+$ dendritic cells (CD11c$^+$ CD11b$^+$), and macrophages (F4/80$^+$ cells) (Fig. 4 D and Table S2). Consistent with an inflammatory response in the germ-free *Rnaset2*$^{-/-}$ mice, serum levels of IP-10 were elevated (Fig. 4 E). Additionally, serum levels of IL-10 also displayed an upward trend in the serum of 8-wk-old germ-free *Rnaset2*$^{-/-}$ mice (Fig. 4 F). Collectively, these results indicate that even in the absence of microbes (germ-free conditions), *Rnaset2*$^{-/-}$ mice exhibit signs of inflammation. Importantly, this inflammatory phenotype shares characteristics with that observed in *Rnaset2*$^{-/-}$ mice housed under specific pathogen–free (SPF) conditions, including hepatosplenomegaly and an increased number and percentage of myeloid cells in the spleen. Therefore, these findings suggest that a putative endogenous TLR13 agonist accumulates in the absence of RNase T2, leading to the initiation of inflammation.

Here, we employed genetically modified mouse models to study the in vivo role of RNase T2 in instigating inflammation. Consistent with previous reports, *Rnaset2*$^{-/-}$ mice present enlarged spleen size accompanied by an increase in myeloid cells (Kettwig et al., 2021). Further characterization revealed that *Rnaset2*$^{-/-}$ mice exhibit a predominantly inflammatory phenotype, which is accompanied by hepatosplenomegaly, peripheral leukocytosis, increased hemophagocytosis, ANA formation,

regenerative anemia, and thrombocytopenia. Interestingly, genetic deletion of the TLR adaptor MyD88 completely attenuated these inflammatory phenotypes, and this was fully phenocopied by the ablation of the RNA-sensing PRR TLR13. Notably, *Rnaset2*$^{-/-}$*; Sting*$^{-/-}$ presented enlarged spleens while having partially reduced numbers of myeloid cells. This suggests that STING signaling may contribute in part to the inflammatory phenotype in *Rnaset2*$^{-/-}$ mice, e.g., as a result of tonic type I IFN signaling dependent on the cGAS–STING pathway. In conclusion, our genetic approach delineates a TLR13-MyD88–signaling cascade that initiates inflammation in the absence of RNase T2. Importantly, these results are corroborated by similar observations reported by Sato and colleagues (Sato et al., 2025).

The absence of RNase T2 has been proposed to result in the accumulation of RNAs in the endosomal compartment (Kettwig et al., 2021; Sato et al., 2025). This accumulation plausibly activates TLR13, driving myeloid cell proliferation and inflammation (Sato et al., 2025). Although the origin and identity of these RNA molecules remain unclear, Sato and colleagues observed that antibiotic treatment ameliorates the TLR13-dependent inflammatory phenotype in *Rnaset2*$^{-/-}$ mice (Sato et al., 2025). They thus suggest that the RNA species accumulating in the absence of RNase T2 are of bacterial origin and act as TLR13 agonists. However, our findings indicate that *Rnaset2*$^{-/-}$ mice housed under germ-free conditions still exhibit an enlarged spleen and liver, increased myeloid cell numbers and percentages in the spleen, and enhanced macrophage numbers—fully replicating the phenotype observed in RNase T2 knockout (KO) mice housed under SPF conditions. We speculate that acute microbiome depletion via antibiotics in SPF-housed mice may reduce PAMPs that contribute to a priming mechanism in the inflammatory process of *Rnaset2*$^{-/-}$ mice, rather than directly triggering TLR13 activation. Indeed, microbiome ablation under non-pathological SPF conditions has been shown to significantly reduce spleen size (Wan et al., 2022). Based on these considerations, we hypothesize that RNase T2 constrains an endogenous ligand that accumulates in *Rnaset2*$^{-/-}$ mice, leading to aberrant activation of the TLR13-MyD88–signaling cascade. The identity of this putative endogenous TLR13 agonist, however, remains unknown. Structural studies have revealed that TLR13 recognizes bacterial ssRNA in a sequence-specific manner. Agonists of TLR13 adopt a stem-loop–like structure essential for receptor activation (Song et al., 2015). Similarly, ssRNA from vesicular stomatitis virus can induce TLR13 dimerization and activation, despite a one-nucleotide difference in its core motif compared with canonical bacterial TLR13 agonists. This nucleotide difference does not impede the formation of the critical stem-loop–like structure required for TLR13 activation (Song et al., 2015), suggesting that ssRNAs capable of adopting similar structural features may serve as TLR13 agonists.

Kettwig et al. recently demonstrated that mouse embryonic fibroblasts derived from *Rnaset2*$^{-/-}$ mice accumulate ribosomal and mitochondrial RNAs (Kettwig et al., 2021). Such endogenous RNAs could theoretically adopt TLR13-activating structures, enabling cell-autonomous receptor stimulation. Nevertheless, our studies show that ex vivo–cultured bone BMDMs do not spontaneously produce inflammatory cytokines. This implies that pathophysiologically relevant TLR13 activation may occur in an unidentified cell type or through phagocytosed material, rather than originating from a cell-autonomous source. Indeed, given the high turnover of erythrocytes in the splenic phagocytic system, TLR13-stimulatory RNA might originate from erythrocyte efferocytosis. The observed increase in hemophagocytosis in *Rnaset2*$^{-/-}$ mice could indicate inefficient clearance of erythrocyte debris. Alternatively, this increase could also be a consequence of chronic inflammation, as seen in models of prolonged TLR7 activation (Akilesh et al., 2019). Furthermore, RNA derived from NETosis may also contribute to the inflammatory response (Herster et al., 2020).

Although we have clearly established the role of a TLR13-MyD88–dependent signaling cascade in driving inflammation in RNase T2–deficient mice, our findings do not contradict those of Kettwig et al., who demonstrated that inhibiting type I IFN signaling alleviates neuroinflammation and neuropathology in *Rnaset2*$^{-/-}$ mice (Kettwig et al., 2021). Type I IFN signaling may act as a priming event that activates various cellular programs, leading to heightened cell activation and responsiveness to the actual triggers of autoimmune diseases (Ivashkiv and Donlin, 2014). The partial reduction of splenomegaly observed in STING-deficient mice, in which homeostatic type I IFN production is reduced, would be in line with such a scenario.

Patients carrying mutations in RNase T2 suffer from a CMV infection-like cystic leukoencephalopathy. To date, the pathogenesis of this disease is not understood. RNase T2 processing of complex ssRNA is required for human TLR7 and TLR8 (Greulich et al., 2019; Ostendorf et al., 2020). In patients carrying hypomorphic mutations of RNase T2, TLR8 signaling is abrogated, suggesting that type I IFN activation has to originate from activation of other RNA sensors. Since TLR13 is not expressed in humans, accumulation of endolysosomal RNAs could aberrantly activate other RNA sensors such as RIG-I and MDA5-driving inflammation in patients where RNase T2 is not functional.

In conclusion, here, we show that RNase T2, in addition to promoting TLR7- and TLR8-mediated pro-inflammatory responses in humans and in mice, plays an important role in limiting erroneous TLR13 activation by degrading a yet undefined endogenous RNA molecule.

Materials and methods

Mouse lines and husbandry

Mice used in this study were housed under SPF conditions (21 ± 1°C, on a 12-h light/dark cycle, with an average humidity level of 55%). All mice were bred and maintained in accordance with animal welfare authorities of the government of Upper Bavaria (application number: 55.2-2532.Vet_02-21-97). Established mouse lines used in this study were previously described: *Tlr13*$^{-/-}$ (Li and Chen, 2012), *Pycard*$^{-/-}$ (Drexler et al., 2012), *Sting*$^{-/-}$ (Jin et al., 2011), *Myd88*$^{-/-}$ (Gais et al., 2012). Note that the *Myd88*$^{-/-}$ mice are mice with a *Myd88*^{LSL} knock in/KO allele that include a floxed transcriptional termination element inserted

between exons 1 and 2, which blocks the transcription and translation of Myd88 and hence creates a functional KO. Analogously, *Ticam1*$^{-/-}$ mice are mice in which a floxed transcriptional termination element has been inserted between exons 1 and 2.

Generation of the *Rnaset2a/Rnaset2b* double-KO mouse line

Rnaset2a; Rnaset2b–deficient mice (*Rnaset2*$^{-/-}$ mice) were generated by CRISPR/Cas9-mediated gene editing in C57BL/6J mouse embryos as described previously (Wefers et al., 2023). Zygotes were microinjected into the male pronucleus with a CRISPR/Cas9 ribonucleoprotein solution consisting of 30 ng/µl SpCas9 protein (IDT), 0.3 µM of crRnaset2-In1 (IDT, binding in intron 1 of Rnaset2a and Rnaset2b), 0.3 µM of crRnaset2-In4 (IDT, binding in intron 4 of Rnaset2a and Rnaset2b), and 0.6 µM tracrRNA (IDT). After microinjection, treated zygotes were transferred into pseudopregnant CD-1 foster animals. To establish the double-KO line, mutant founder animals carrying both deletions were identified and subsequently crossed to C57BL/6J animals to isolate the respective allele. Cis-targeting was analyzed in F1 animals by PCR, and the targeted loci were validated by PCR and Sanger sequencing. To exclude unwanted additional modifications, putative off-target sites of the *Rnaset2a/Rnaset2b*–targeting crRNAs were predicted using the CRISPOR online tool (Concordet and Haeussler, 2018). Predicted loci were PCR-amplified and verified by Sanger sequencing. Validated animals without any off-target mutations were used for further breeding.

For gene-targeting, the following crRNAs were used: crRnaset2-In1 (Protospacer+PAM): 5′-CAGTATGTGTGCATGCGACAAGG-3′, crRnaset2-In4 (Protospacer+PAM): 5′-TAGGGCATGTTCCTGCTAGGGGG-3′. For genotyping and sequencing the following oligos were used: Rnaset2a-In1-fw: 5′-GTTCTGGGATTAAAATTGTGTCTTCC-3′, Rnaset2a-In4-rv: 5′-CCTGTCCTGAATGAATGAATGAATG-3′, Rnaset2b-In1-fw: 5′-GCCACGTCCATCTCGATCTC-3′ and Rnaset2b-In4-rv: 5′-GAAAAACCCTGTCCCGAATAAAT-3′.

All animal experiments were approved by the Bavarian government under license number ROB-55.2Vet-2532.Vet_02-16-121. All mice were handled according to institutional guidelines approved by the animal welfare and use committee of the government of Upper Bavaria and housed in standard cages in a SPF facility on a 12-h light/dark cycle with ad libitum access to food and water.

Genotyping of mouse lines used in the study

Genomic DNA from Proteinase K–digested ear tissue was extracted using a 100 mM Tris-HCL (pH 8.0); 200 mM NaCl; SDS (0.2%); and 5 mM EDTA (pH 8.0)-based buffer. The primers used for the PCR reactions are the following: *Rnaset2a* (*Rnaset2a* common fwd: 5′-GTTCTGGGATTAAAATTGTGTCTTCC-3′, *Rnaset2a/b* WT rev: 5′-GCCTTTTTCACGGTGCTCAG-3′, and *Rnaset2a* KO rev: 5′-CCTGTCCTGAATGAATGAATGAATG-3′). *Rnaset2b* (*Rnaset2b* common fwd: 5′-GCCACGTCCATCTCGATCTC-3′, *Rnaset2a/b* WT rev: 5′-GCCTTTTTCACGGTGCTCAG-3′, and *Rnaset2b* KO rev: 5′-GAAAAACCCTGTCCCGAATAAAT-3′). *Myd88* (*Myd88* common fwd: 5′-GCGTCAGATCTCATTATGGG-3′, *Myd88* WT rev: 5′-GAAGGGTGTAGAGGCTCCTC-3′, and *Myd88* KO rev: 5′-CCACCCTGGGGTTCGTGTCC-3′). *Pycard* (*Pycard* common fwd: 5′-GGCTTAGTGTTCTAGCTGTT-3′, *Pycard* WT rev: 5′-ACCAGGAAGTCAGCTGCTTA-3′, and *Pycard* KO rev: 5′-TTCACACAATACGATCTTCA-3′). *Sting* (*Sting* common fwd: 5′-CCTCTCCTAGACAGGTGCTG-3′, *Sting* WT rev: 5′-TGATTTGGTGGATCCTTTGC-3′, and *Sting* KO rev: 5′-CGGCCGAAGTTCCTATTCTC-3′). *Tlr13* (*Tlr13* WT fwd: 5′-GAAGCTATCCAGTCATGGTAGAC-3′, *Tlr13* WT rev: 5′-TTCCTTTCACTGAAGCACTAACTC-3′, *Tlr13* KO fwd: 5′-GTTGAGAGCCAAGGGAGAAG-3′, and *Tlr13* KO rev: 5′-GTCTGTCCTAGCTTCCTCACTG-3′). *Ticam1* (*Ticam1* common fwd: 5′-TCTGCAGCACTGACCCGCTG-3′, *Ticam1* WT rev: 5′-GACCCTGGCCTCCGTGTCCT-3′, and *Ticam1* KO rev: 5′-CCACCCTGGGGTTCGTGTCC-3′).

Rederivation of germ-free mice and germ-free housing conditions

For rederivation, colonized (SPF) *Rnaset2*$^{-/-}$ mice were mated (timed pregnancy), and then, only a few hours before natural birth, the aseptic hysterectomy was performed: The gravid uterus was removed and passed through a germicidal dip tank into the isolator, where the germ-free neonates were raised by a germ-free dam. Germ-free mice were obtained from the Central Animal Facility (Hannover Medical School, Hannover, Germany) and maintained in plastic film isolators (Metall + Plasstik GmbH). The germ-free mice were housed on a 12-h light/dark cycle, 21 ± 1°C. Health monitoring of the germ-free mice was performed according to Federation of European Laboratory Animal Science Associations and recommendations for maintaining germ-free colonies. Germ-free mice were proved to be free of contaminants or infections (Nicklas et al., 2015). Mice received pelleted 50 kGy gamma-irradiated feed (Complete feed for mice—breeding [M-Z], V1124-927; Ssniff Spezialdiäten GmbH) and autoclaved water ad libitum. At the age of 8 and 26 wk, the mice were sacrificed by CO_2 inhalation followed by exsanguination via cardiopuncture. All procedures were approved by the local institutional Animal Care and Research Advisory committee and permitted by the Lower Saxony State Office for Consumer Protection and Food Safety or the local veterinary authorities (reference numbers: 42500/1H, 23-00350, and 2023-242).

Flow cytometry

Immunophenotyping of spleen cells

Spleens were harvested and homogenized, and RBCs were lysed using ammonium–chloride–potassium lysis buffer. Cells were then washed and incubated with FcR blocking reagent (130-092-575; Miltenyi Biotec) at 4°C for 10–15 min. The following antibodies were used for staining: CD45 (109838, 4 µg/ml; BioLegend), CD3 (100330, 4 µg/ml; BioLegend), CD4 (100456, 2 µg/ml; BioLegend), CD8 (140418, 2 µg/ml; BioLegend), CD11c (117320, 2.5 µg/ml; BioLegend), I-A^b (116418, 4 µg/ml; BioLegend), CD19 (115520, 1 µg/ml; BioLegend), Nkp46 (137612, 4 µg/ml; BioLegend), CD11b (101219, 2.5 µg/ml; BioLegend), F4/80 (123141, 0.8 µg/ml; BioLegend), and Ly6G (127639, 1 µg/ml; BioLegend). The samples were analyzed on an LSR Fortessa flow cytometer (BD), and data were processed using FlowJo software.

Staining of Ter-119 within macrophages

Spleens from 40–54-wk-old mice were harvested and homogenized, and RBCs were lysed using ammonium–chloride–potassium lysis buffer. Cells were then washed and incubated with FcR blocking reagent at 4°C for 10–15 min. Subsequently, cells were stained for the extracellular markers CD45 (109838; 4 µg/ml; BioLegend), CD169 (142403; 2.5 µg/ml; BioLegend), and F4/80 (123141; 0.8 µg/ml; BioLegend) for 30 min at 4°C. Following this, cells were washed and prepared for intracellular staining using the Fixation and Permeabilization buffer (BD Biosciences). Cells were fixed and permeabilized with the Perm/Wash Buffer kit (BD Biosciences) according to the manufacturer's instructions and then stained with fluorescently labeled anti–Ter-119 (116211; 5 µg/ml; BioLegend) to detect cells that had phagocytosed RBCs.

Blood analysis

Blood was withdrawn from the submandibular vein using a lancet and collected into a BD Microtainer K2E tube. Immediately after the blood parameters were determined using an Idexx hematology analyzer.

Cytokine analysis

To measure cytokine levels in the serum of the mice, the Multi-Analyte Flow Assay Kit (Legendplex, 740621; BioLegend) was used. For mice kept under SPF conditions, the blood was withdrawn from the submandibular vein using a lancet. For mice rederived under germ-free conditions, the mice were deeply anesthetized with 150 µg/g ketamine and 15 µg/g xylazine, and the blood was withdrawn from the vena cava using a 25-gauge needle. Immediately after collection, the blood was transferred to a BD Microtainer K2E tube to prevent coagulation. Subsequently, the blood was centrifuged at 12,000 × *g* for 6 min, and the serum was collected and stored at −80°C until further analysis. Samples were measured in duplicates following the manufacturer's instructions and analyzed on an LSR Fortessa flow cytometer (BD).

Isolation and stimulation of BMDMs

The bone marrow cells from the tibia and femur of 8–12-wk-old mice were flushed and differentiated in DMEM, supplemented with 10% FCS and 30% L-929–conditioned media for 6–7 days. BMDMs (80,000 cells/well in a 96-well plate) were transfected with RNA40 or Sa19 as indicated. RNA oligonucleotides and poly-L-arginine were incubated separately with pre-warmed Opti-MEM (25 µl/well) in a 1:1 ratio for 5 min. Next, the two reagents were combined and incubated for an additional 20 min at room temperature (RT) and immediately added to the cells. The supernatant of BMDMs was harvested 16 h after transfection.

Detection of ANAs

Sera were screened for ANAs by immunofluorescence analysis on murine 3T3 fibroblasts at a 1:80 dilution. 3T3 cells were cultured in DMEM with 10% FCS, seeded into chamber slides (Ibidi), and grown overnight. Cells were fixed and permeabilized by incubation in cold (−20°C) methanol for 8 min, followed by cold acetone for 2 min. Slides were then washed with PBS and blocked with 1% BSA and 0.1% Tween 20 in PBS for 60 min before incubation with the serum dilution (in blocking buffer) overnight at 4°C. The anti-double-stranded DNA monoclonal IgG antibody BV16-13 (Sigma-Aldrich) served as a positive control. After washing, bound IgG was detected by incubation with a goat anti-mouse IgG cross-absorbed secondary antibody conjugated to Alexa Fluor 488 for 1 h at RT. Slides were covered with mounting medium containing DAPI and analyzed by confocal microscopy using a Nikon A1R instrument. For sera that showed nuclear staining at 1:80, the assay was repeated with a twofold dilution series (up to 1:20480). The titer was defined as the highest dilution that yielded detectable nuclear staining.

Histology of brain tissue

Tissue preparation

Mice were anesthetized with an intraperitoneal injection of ketamine/xylazine. The chest was then opened, and a cannula was inserted into the left ventricle of the heart for transcardial perfusion with ice-cold saline containing 0.5% heparin. Following perfusion, the brain was removed from the skull and stored in 5% paraformaldehyde overnight at 4°C. After fixation, the brain was rinsed in PBS and embedded in 4% agarose gel for coronal sectioning using a vibratome (VT 1200S; Leica). Coronal sections were collected at a thickness of 50 µm, spanning from 2.5 mm anterior to bregma to 6.5 mm posterior to bregma. Sections at +1.5-, 0-, and −1.5-mm bregma were separated for immunofluorescence staining and cell type quantification.

Tissue staining

To identify the cellular impact of RNase T2 deficiency on neurons and glia, NeuN (neuronal marker) was co-labeled with Iba1 (microglia marker) and DAPI (nuclear marker) in slices from different populations of mouse age cohorts. All free-floating sections were washed twice for 10 min in 1x PBS before permeabilization with 0.1% Triton X-100 and 0.05% Tween 20 in PBS for 30 min. Nonspecific protein-binding sites were blocked with a combination of 1% BSA, 0.1% fish-skin gelatin, and 2% normal donkey serum in 1x PBS for 1 h at RT. Slices were incubated with primary antibodies overnight at 4°C (anti-Iba1: goat, 011–27991; Wako, 1:200; anti-NeuN: rabbit, 177487, 1:200; Abcam) in a mixture of 1% BSA and 0.5% Triton X-100 in 1x PBS. After three washes for 10 min each at RT, secondary antibodies were applied for 1 h at RT (anti-rabbit: Alexa 594, donkey, A21207; Invitrogen, 1:200; anti-goat: Alexa 647, donkey, A21447, 1:200; Invitrogen) in 1% BSA in 1x PBS. This process was followed by another three washes in 1x PBS at RT, and then all sections were incubated in DAPI (1:5,000 in 1x PBS) for 2 min, followed by another two washes. Slices were mounted with Fluoromount Aqueous mounting medium (F4680; Sigma-Aldrich) and covered with #1.5 coverslips (Ependia) before air drying.

Image acquisition and analysis

Confocal tile scan images of the entire section were taken using a 10× Apochromatic Objective with a Zeiss LSM880 inverted confocal microscope (Carl Zeiss GmbH) and were processed and

assembled using a custom-built macro in ImageJ (National Institutes of Health). For image processing, all high-resolution images were first scaled, aligned, and contrast adjusted to each other. All images were renamed to blind the researcher to the group. Using the Iba1-647 channel to evaluate neuroinflammatory hotspots in the brain, clusters were manually marked on the images and quantified. This was followed by a subregional analysis to estimate neuronal loss in the areas with inflammation. Since Iba1 clusters appeared sporadically throughout the brain, we limited the quantification to one cortical and one subcortical region on each of the coronal brain sections, yielding a maximum of six regions of interest (ROIs) per mouse. Every ROI was then normalized to the contralateral hemisphere homotypic brain area, showing percentage changes that were subsequently quantified.

Steps of subregional image analysis

An ROI of 0.2 square mm was used. Images were cropped, binarized (auto threshold with Phansalkar filter), despeckled, and subjected to watershed segmentation. NeuN-positive cells were quantified using the analyze particles function in ImageJ. In the WT mice, one cortical and one subcortical area were selected as references, without Iba1$^+$ clusters, to serve as a baseline.

CO-Detection by IndEXing (CODEX) multiplexed imaging of tissue using DNA-conjugated antibodies

Antibody conjugation, tissue preparation, and staining of fixed frozen spleen samples for multicycle CODEX (now known as PhenoCycler) are related to the Nolan lab protocol (Black et al., 2021).

Antibody conjugation

50-kDa Amicon Ultra filters (UFC505096; Thermo Fisher Scientific) were blocked with 0.1% PBS-Tween. Following blocking, carrier-free, purified antibodies were added to the column. After centrifugation, antibodies were reduced for 30 min using tris(2-carboxyethyl)phosphine (TCEP) solution (2.5 mM TCEP and 2.5 mM EDTA in 1x Dulbecco's phosphate-buffered saline (DPBS), pH 7.0). After reduction, antibodies were washed using Buffer C (Tris buffer containing 1 mM Tris [pH 7.0], 1 mM Tris [pH 7.5], 150 mM NaCl, 1 mM EDTA [pH 8.0], and 0.02% [wt/vol] NaN_3). Reduced antibodies were then incubated with maleimide-modified oligonucleotides (Biomers) in a 2:1 (wt/wt) ratio. Maleimide-modified oligonucleotides were provided lyophilized and reconstituted immediately before use in 1x DPBS in the vapor phase of LN_2. After a 2-h incubation, the antibody-oligonucleotide solution was washed three times with high-salt PBS (1 M NaCl and 0.02% [wt/vol] NaN_3 in 1x DPBS). Antibodies were reconstituted to a final concentration of 0.5 mg/ml in a working antibody stabilizer solution containing 500 mM NaCl, 5 mM EDTA, and 0.2% (wt/vol) NaN_3 in antibody stabilizer solution (Candor). Antibodies were stored at 4°C.

Tissue preparation

Mouse spleens were harvested and two crosssections were performed. The tissues were then immediately fixed for 4–6 h at 4°C using a 1:4 dilution of BD Cytofix/Cytoperm (554722; BD Biosciences) in 1x DPBS. Following fixation, the tissues were washed twice in 1x DPBS for 5 min. Afterward, the tissues were dehydrated using a sucrose solution. Dehydration was performed for 2 h at 4°C using 30% (wt/vol) sucrose in 1x DPBS followed by 16 h using 50% (wt/vol) sucrose in 1x DPBS. After dehydration, the tissues were embedded Tissue-Tek O.C.T. Compound (4583; Sakura Finetek) and frozen on dry ice. Tissues were stored at −80°C until sectioning.

Tissue staining

Fixed frozen mouse spleen samples were sectioned at 5 µm using a cryostat. Sections were immediately mounted onto poly-L-lysine–coated coverslips and kept on dry ice until staining (maximum 1 h after sectioning). Sections were placed in a container with Drierite beads to absorb excess moisture. Tissues were rehydrated for 4 min at RT in 1x TBS immunohistochemistry wash buffer with Tween 20 (28360; Thermo Fisher Scientific). Following rehydration, tissues were blocked and stained. Blocking was performed with 100 µl blocking buffer per coverslip, containing 1 mg/ml mouse IgG (I5381; Sigma-Aldrich), 1 mg/ml rat IgG (I4131; Sigma-Aldrich), 10 mg/ml sheared salmon sperm DNA (AM9680; Invitrogen), and 0.05 mM naked oligonucleotide (Biomers) diluted in S2 buffer (61 mM Na_2HPO_4, 39 mM Na_2HPO_4, 250 mM NaCl, and 250 ml S1 buffer [5 mM EDTA, 0.5% (wt/vol) BSA, and 0.02% (wt/vol) NaN_3 in 1x DPBS] in a total volume of 500 ml double-distilled water (ddH_2O), pH 6.8–7.0).

The antibody-staining solution was prepared in blocking buffer. For this, 0.5–4 µl of each antibody (0.5 mg/ml stock solution of maleimide-conjugated antibodies) was added to 50 µl blocking buffer (refer to antibody list for details). Before adding the antibody solution to the blocked tissue sections, the antibody master mix was filtered through a 50-kDa Amicon Ultra filter unit and reconstituted in 100 µl blocking buffer. Tissues were incubated with the antibody-staining solution overnight at 4°C in a humidity chamber. The following day, tissues were washed twice in S2 buffer and subjected to a three-step fixation process: first, 10 min at RT with 1.6% paraformaldehyde in S4 buffer (1x DPBS containing 0.5 M NaCl, 5 mM EDTA, 0.5% [wt/vol] BSA, and 0.02% [wt/vol] NaN_3), followed by 5 min in ice-cold methanol, and finally 20 min at RT in 8 mM bis(sulfosuccinimidyl)suberate (21580; Thermo Fisher Scientific). After each fixation step, tissues were washed three times in 1x DPBS. Tissues were stored in S4 buffer until image acquisition.

The antibodies used for staining were as follows: Ki67 (556003, 10 µg/ml; BD Biosciences), CD169 (142402, 2.5 µg/ml; BioLegend), CD11b (101202, 2.5 µg/ml; BioLegend), Ly6G (127602, 2.5 µg/ml; BioLegend), and F4/80 (565409, 1.25 µg/ml; BD Biosciences).

Image acquisition and analysis

Tissue sections were acquired using multicycle CODEX technology in combination with a Zeiss Axio Observer 7 inverted microscope equipped with a Colibri 7 LED light source (Carl Zeiss) and a Prime BSI PCIe camera (Teledyne Photometrics). Complementary fluorescent oligonucleotides (Biomers) at a final concentration of 400 nM were aliquoted into Corning

black 96-well plates with 250 µl of plate buffer (150 mM NaCl, 10 mM Tris, pH 7.5, 10 mM $MgCl_2$ 6 H_2O, 0.1% [wt/vol] Triton X-100, and 0.02% [wt/vol] NaN_3 in ddH_2O), 0.015 mM DAPI (422801; BioLegend), and 0.5 mg/ml sheared salmon sperm DNA. Interactive imaging cycles were performed using an Akoya CODEX instrument and CODEX Instrument Manager software (Akoya Biosciences). Automated image acquisition was conducted with the Plan-Apochromat 20×/0.8 M27 (a = 0.55 mm) objective (Carl Zeiss), and the imaging pipeline was controlled by a focus strategy with autofocus for each support point, generating a three z-stack image with a 1.5-µm distance between each z-stack. DAPI nuclear stain was imaged in each cycle.

Following acquisition, images were processed with CODEX Processor Version 1.8.3.14 (Akoya Biosciences) and analyzed using HALO Image Analysis software (Indica Labs). Cell segmentation, identification of various cell populations, and distinct tissue features were performed using implemented software packages (Nuclei Seg Plugin and Random Forest algorithm supported by an artificial intelligence module for nucleus and membrane identification). Tissue artifacts, such as folds, were excluded from the analysis. A Random Forest classifier was used to define different zones (white pulp, RP, and marginal zone), employing a decision tree approach to classify pixels based on user-provided training examples. RP macrophages were defined as $DAPI^+$; $F4/80^+$; $CD169^-$; $Ly6G^-$; ± Ki67 cells, and CD169 macrophages were defined as $DAPI^+$; $CD169^+$; $F4/80^-$; $Ly6G^-$; ± Ki67 cells.

Quantification and statistical analysis

Statistical analysis was performed with Prism software (GraphPad). The specific number of replicates, denoted as (*n*), is indicated in the figure or in the legends accompanying each figure, while the statistical test used is indicated in the accompanying legend. In cases where a comparison bar is used to illustrate multiple comparisons, the extended line on the bar indicates the reference data set to which the significance level information applies. Flow cytometry data were analyzed and plotted using FlowJo software.

Online supplemental material

Fig. S1 shows the gating strategy used to identify immune cell populations in the spleens of WT and *Rnaset2*$^{-/-}$ mice. It also presents serum cytokine levels in aged WT and *Rnaset2*$^{-/-}$ mice. Fig. S2 illustrates the spleen architecture in WT, *Rnaset2*$^{-/-}$, and *Rnaset2*$^{-/-}$*; Myd88*$^{-/-}$ mice. It also depicts cytokine production by WT and *Rnaset2*$^{-/-}$ macrophages stimulated with various PRR agonists. Fig. S3 demonstrates the neuroinflammation in *Rnaset2*$^{-/-}$ mice, including $Iba1^+$ staining and quantification. It also shows hepatomegaly in germ-free mice. Table S1 provides the quantification of splenic immune cell populations in young and aged WT and *Rnaset2*$^{-/-}$ mice. Table S2 provides the quantification of splenic immune cell populations in germ-free WT and *Rnaset2*$^{-/-}$ mice.

Data availability

All data in the article and its supplementary materials are available upon request from the corresponding author.

Acknowledgments

We thank Clara Ludwig (BioSysM flow cytometry facility), Larissa Hansbauer, Kristin Leike, and Jochen Rech from the Hornung lab for their great technical assistance. We thank animal caretakers of the gnotobiotic unit and Anna Smoczek at the Central Animal Facility of the Hannover Medical School for their excellent technical assistance. We kindly thank Zhijian Chen (University of Texas Southwestern Medical Center) for allowing us to work with *Tlr13*-deficient mice and Carsten Kirschning (Universitätsklinikum Essen, Essen, Germany) for providing us with these mice.

This work was supported by grants from the European Research Council (ERC-2020-ADG–101018672 ENGINES) to V. Hornung, and the Deutsche Forschungsgemeinschaft (DFG, German Research Foundation) CRC 237/A27 (Project-ID 369799452) to V. Hornung and CRC 237/B17 to A. Roers, as well as the DFG grant CRC 1371 (project ID 395357507) to M. Basic.

Author contributions: C. Gomez-Diaz: conceptualization, data curation, formal analysis, investigation, methodology, validation, and writing—original draft, review, and editing. W. Greulich: conceptualization, data curation, formal analysis, investigation, methodology, project administration, and validation. B. Wefers: methodology and resources. M. Wang: data curation, investigation, methodology, and writing—review and editing. S. Bolsega: investigation, methodology, resources, and writing—review and editing. M. Effern: formal analysis, investigation, and methodology. D.P. Varga: data curation, formal analysis, investigation, methodology, visualization, and writing—original draft. Z. Han: investigation. M. Chen: investigation. M. Bérouti: investigation. N. Leonardi: formal analysis and investigation. U. Schillinger: resources. B. Holzmann: resources and writing—review and editing. A. Liesz: funding acquisition, supervision, and validation. A. Roers: investigation, supervision, and visualization. M. Holzel: project administration, resources, supervision, and writing—review and editing. M. Basic: funding acquisition, investigation, methodology, project administration, resources, and writing—review and editing. W. Wurst: conceptualization, funding acquisition, methodology, resources, and writing—original draft. V. Hornung: conceptualization, data curation, formal analysis, funding acquisition, project administration, resources, supervision, validation, visualization, and writing—original draft, review, and editing.

Disclosures: W. Wurst reported a patent (WO2014/131833) issued: "Generation of mouse models using CRISPR/Cas9 in zygotes is patented (WO2014/131833)." No other disclosures were reported.

Submitted: 11 August 2024
Revised: 18 November 2024
Accepted: 20 December 2024

References

Akilesh, H.M., M.B. Buechler, J.M. Duggan, W.O. Hahn, B. Matta, X. Sun, G. Gessay, E. Whalen, M. Mason, S.R. Presnell, et al. 2019. Chronic TLR7 and TLR9 signaling drives anemia via differentiation of specialized hemophagocytes. *Science*. 363:eaao5213. https://doi.org/10.1126/science.aao5213

Berouti, M., K. Lammens, M. Heiss, L. Hansbauer, S. Bauernfried, J. Stockl, F. Pinci, I. Piseddu, W. Greulich, M. Wang, et al. 2024. Lysosomal

endonuclease RNase T2 and PLD exonucleases cooperatively generate RNA ligands for TLR7 activation. *Immunity*. 57:1482–1496.e8. https://doi.org/10.1016/j.immuni.2024.04.010

Black, S., D. Phillips, J.W. Hickey, J. Kennedy-Darling, V.G. Venkataraaman, N. Samusik, Y. Goltsev, C.M. Schürch, and G.P. Nolan. 2021. CODEX multiplexed tissue imaging with DNA-conjugated antibodies. *Nat. Protoc.* 16:3802–3835. https://doi.org/10.1038/s41596-021-00556-8

Concordet, J.P., and M. Haeussler. 2018. CRISPOR: Intuitive guide selection for CRISPR/Cas9 genome editing experiments and screens. *Nucleic Acids Res.* 46:W242–W245. https://doi.org/10.1093/nar/gky354

Crow, Y.J., and D.B. Stetson. 2022. The type I interferonopathies: 10 years on. *Nat. Rev. Immunol.* 22:471–483. https://doi.org/10.1038/s41577-021-00633-9

Drexler, S.K., L. Bonsignore, M. Masin, A. Tardivel, R. Jackstadt, H. Hermeking, P. Schneider, O. Gross, J. Tschopp, and A.S. Yazdi. 2012. Tissue-specific opposing functions of the inflammasome adaptor ASC in the regulation of epithelial skin carcinogenesis. *Proc. Natl. Acad. Sci. USA.* 109:18384–18389. https://doi.org/10.1073/pnas.1209171109

Fitzgerald, K.A., and J.C. Kagan. 2020. Toll-like receptors and the control of immunity. *Cell*. 180:1044–1066. https://doi.org/10.1016/j.cell.2020.02.041

Gais, P., D. Reim, G. Jusek, T. Rossmann-Bloeck, H. Weighardt, K. Pfeffer, F. Altmayr, K.P. Janssen, and B. Holzmann. 2012. Cutting edge: Divergent cell-specific functions of MyD88 for inflammatory responses and organ injury in septic peritonitis. *J. Immunol.* 188:5833–5837. https://doi.org/10.4049/jimmunol.1200038

Greulich, W., M. Wagner, M.M. Gaidt, C. Stafford, Y. Cheng, A. Linder, T. Carell, and V. Hornung. 2019. TLR8 is a sensor of RNase T2 degradation products. *Cell*. 179:1264–1275.e13. https://doi.org/10.1016/j.cell.2019.11.001

Henneke, M., S. Diekmann, A. Ohlenbusch, J. Kaiser, V. Engelbrecht, A. Kohlschütter, R. Krätzner, M. Madruga-Garrido, M. Mayer, L. Opitz, et al. 2009. RNASET2-deficient cystic leukoencephalopathy resembles congenital cytomegalovirus brain infection. *Nat. Genet.* 41:773–775. https://doi.org/10.1038/ng.398

Herster, F., Z. Bittner, N.K. Archer, S. Dickhöfer, D. Eisel, T. Eigenbrod, T. Knorpp, N. Schneiderhan-Marra, M.W. Löffler, H. Kalbacher, et al. 2020. Neutrophil extracellular trap-associated RNA and LL37 enable self-amplifying inflammation in psoriasis. *Nat. Commun.* 11:105. https://doi.org/10.1038/s41467-019-13756-4

Ivashkiv, L.B., and L.T. Donlin. 2014. Regulation of type I interferon responses. *Nat. Rev. Immunol.* 14:36–49. https://doi.org/10.1038/nri3581

Jin, L., K.K. Hill, H. Filak, J. Mogan, H. Knowles, B. Zhang, A.L. Perraud, J.C. Cambier, and L.L. Lenz. 2011. MPYS is required for IFN response factor 3 activation and type I IFN production in the response of cultured phagocytes to bacterial second messengers cyclic-di-AMP and cyclic-di-GMP. *J. Immunol.* 187:2595–2601. https://doi.org/10.4049/jimmunol.1100088

Kettwig, M., K. Ternka, K. Wendland, D.M. Krüger, S. Zampar, C. Schob, J. Franz, A. Aich, A. Winkler, M.S. Sakib, et al. 2021. Interferon-driven brain phenotype in a mouse model of RNaseT2 deficient leukoencephalopathy. *Nat. Commun.* 12:6530. https://doi.org/10.1038/s41467-021-26880-x

Li, X.D., and Z.J. Chen. 2012. Sequence specific detection of bacterial 23S ribosomal RNA by TLR13. *Elife*. 1:e00102. https://doi.org/10.7554/eLife.00102

Lind, N.A., V.E. Rael, K. Pestal, B. Liu, and G.M. Barton. 2022. Regulation of the nucleic acid-sensing Toll-like receptors. *Nat. Rev. Immunol.* 22:224–235. https://doi.org/10.1038/s41577-021-00577-0

Mouat, I.C., E. Goldberg, and M.S. Horwitz. 2022. Age-associated B cells in autoimmune diseases. *Cell. Mol. Life Sci.* 79:402. https://doi.org/10.1007/s00018-022-04433-9

Nicklas, W., L. Keubler, and A. Bleich. 2015. Maintaining and monitoring the defined microbiota status of gnotobiotic rodents. *ILAR J.* 56:241–249. https://doi.org/10.1093/ilar/ilv029

Nusser, A., N. Nuber, O.F. Wirz, H. Rolink, J. Andersson, and A. Rolink. 2014. The development of autoimmune features in aging mice is closely associated with alterations of the peripheral CD4$^+$ T-cell compartment. *Eur. J. Immunol.* 44:2893–2902. https://doi.org/10.1002/eji.201344408

Oldenburg, M., A. Krüger, R. Ferstl, A. Kaufmann, G. Nees, A. Sigmund, B. Bathke, H. Lauterbach, M. Suter, S. Dreher, et al. 2012. TLR13 recognizes bacterial 23S rRNA devoid of erythromycin resistance-forming modification. *Science*. 337:1111–1115. https://doi.org/10.1126/science.1220363

Ostendorf, T., T. Zillinger, K. Andryka, T.M. Schlee-Guimaraes, S. Schmitz, S. Marx, K. Bayrak, R. Linke, S. Salgert, J. Wegner, et al. 2020. Immune sensing of synthetic, bacterial, and Protozoan RNA by toll-like receptor 8 requires coordinated processing by RNase T2 and RNase 2. *Immunity*. 52:591–605.e6. https://doi.org/10.1016/j.immuni.2020.03.009

Rice, G.I., I. Melki, M.L. Frémond, T.A. Briggs, M.P. Rodero, N. Kitabayashi, A. Oojageer, B. Bader-Meunier, A. Belot, C. Bodemer, et al. 2017. Assessment of type I interferon signaling in pediatric inflammatory disease. *J. Clin. Immunol.* 37:123–132. https://doi.org/10.1007/s10875-016-0359-1

Sato, R., K. Liu, T. Shibata, K. Hoshino, K. Yamaguchi, T. Miyazaki, R. Hiranuma, R. Fukui, Y. Motoi, Y. Fukuda-Ohta, et al. 2025. RNaseT2-deficiency promotes TLR13-dependent replenishment of tissue-protective Kupffer cells. *J. Exp. Med.* https://doi.org/10.1084/jem.20230647

Song, W., J. Wang, Z. Han, Y. Zhang, H. Zhang, W. Wang, J. Chang, B. Xia, S. Fan, D. Zhang, et al. 2015. Structural basis for specific recognition of single-stranded RNA by Toll-like receptor 13. *Nat. Struct. Mol. Biol.* 22:782–787. https://doi.org/10.1038/nsmb.3080

Tanji, H., U. Ohto, T. Shibata, M. Taoka, Y. Yamauchi, T. Isobe, K. Miyake, and T. Shimizu. 2015. Toll-like receptor 8 senses degradation products of single-stranded RNA. *Nat. Struct. Mol. Biol.* 22:109–115. https://doi.org/10.1038/nsmb.2943

Wan, X., A. Eguchi, A. Sakamoto, Y. Fujita, Y. Yang, Y. Qu, M. Hatano, C. Mori, and K. Hashimoto. 2022. Impact of broad-spectrum antibiotics on the gut-microbiota-spleen-brain axis. *Brain Behav. Immun. Health*. 27:100573. https://doi.org/10.1016/j.bbih.2022.100573

Wefers, B., W. Wurst, and R. Kühn. 2023. Gene editing in mouse zygotes using the CRISPR/Cas9 system. *Methods Mol. Biol.* 2631:207–230. https://doi.org/10.1007/978-1-0716-2990-1_8

Yamamoto, M., S. Sato, H. Hemmi, K. Hoshino, T. Kaisho, H. Sanjo, O. Takeuchi, M. Sugiyama, M. Okabe, K. Takeda, and S. Akira. 2003. Role of adaptor TRIF in the MyD88-independent toll-like receptor signaling pathway. *Science*. 301:640–643. https://doi.org/10.1126/science.1087262

Yamamoto, M., S. Sato, K. Mori, K. Hoshino, O. Takeuchi, K. Takeda, and S. Akira. 2002. Cutting edge: A novel toll/IL-1 receptor domain-containing adapter that preferentially activates the IFN-beta promoter in the toll-like receptor signaling. *J. Immunol.* 169:6668–6672. https://doi.org/10.4049/jimmunol.169.12.6668

JEM

Supplemental material

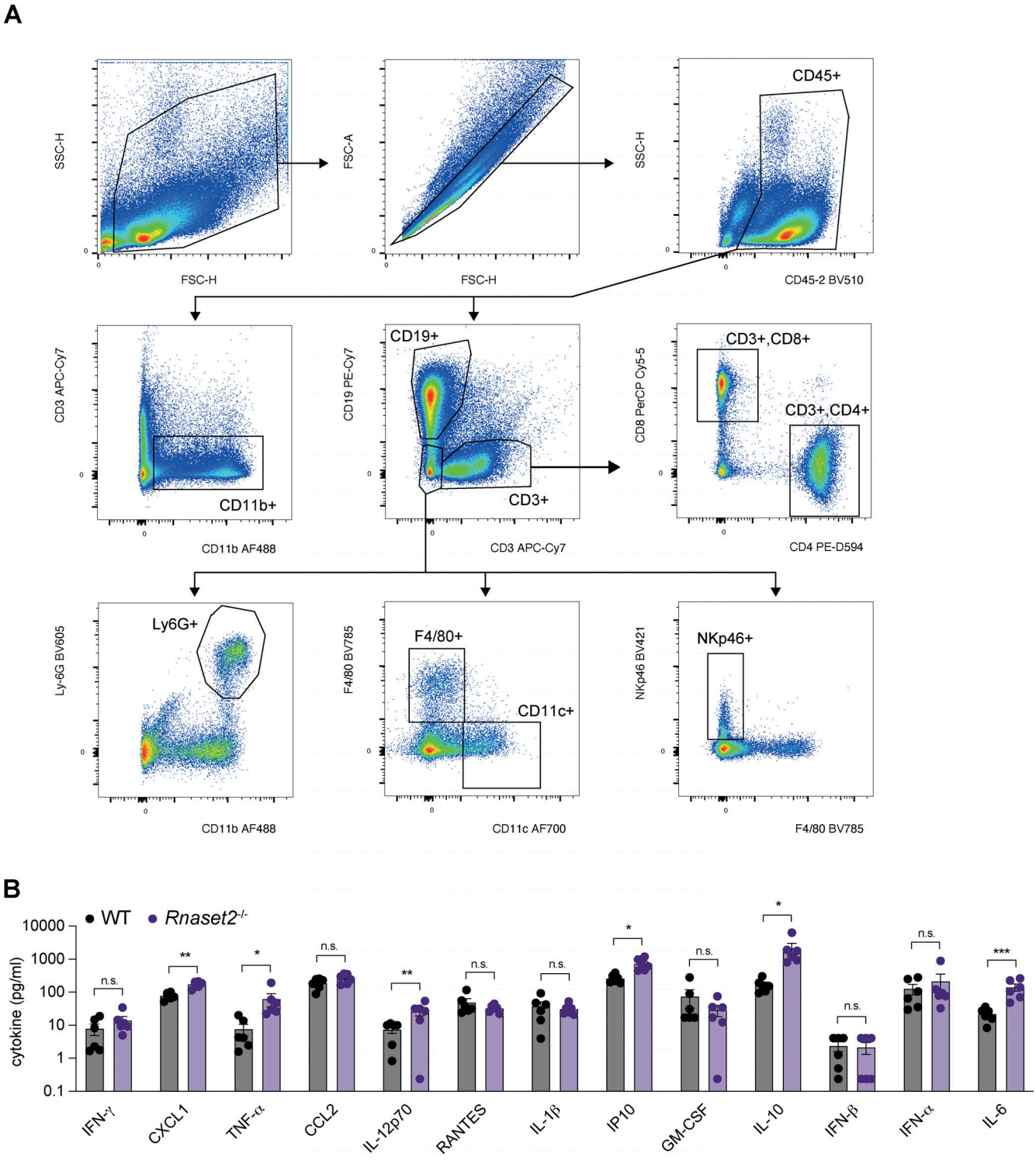

Figure S1. **Immune cell populations in spleens of WT and *Rnaset2*$^{-/-}$ mice. (A)** Representative gating strategy to determine the percentages of various immune cells within the spleen. Arrows indicate the populations further analyzed in the subsequent gates. Data shown are from a representative *Rnaset2*-deficient mouse. **(B)** Serum cytokine levels in 40–54-wk-old mice of the indicated genotypes (WT $n = 6$, *Rnaset2*$^{-/-}$ $n = 6$). Data are shown as mean ± SEM; statistical analysis was performed using a one-way ANOVA with Dunnett's correction for all genotypes, except for GM-CSF, IFNβ, and IFNα, where an unpaired two-tailed *t* test was applied due to the analysis of only two genotype groups. Significance levels are indicated as *P < 0.05, **P < 0.01, and ***P < 0.001; n.s. = not significant.

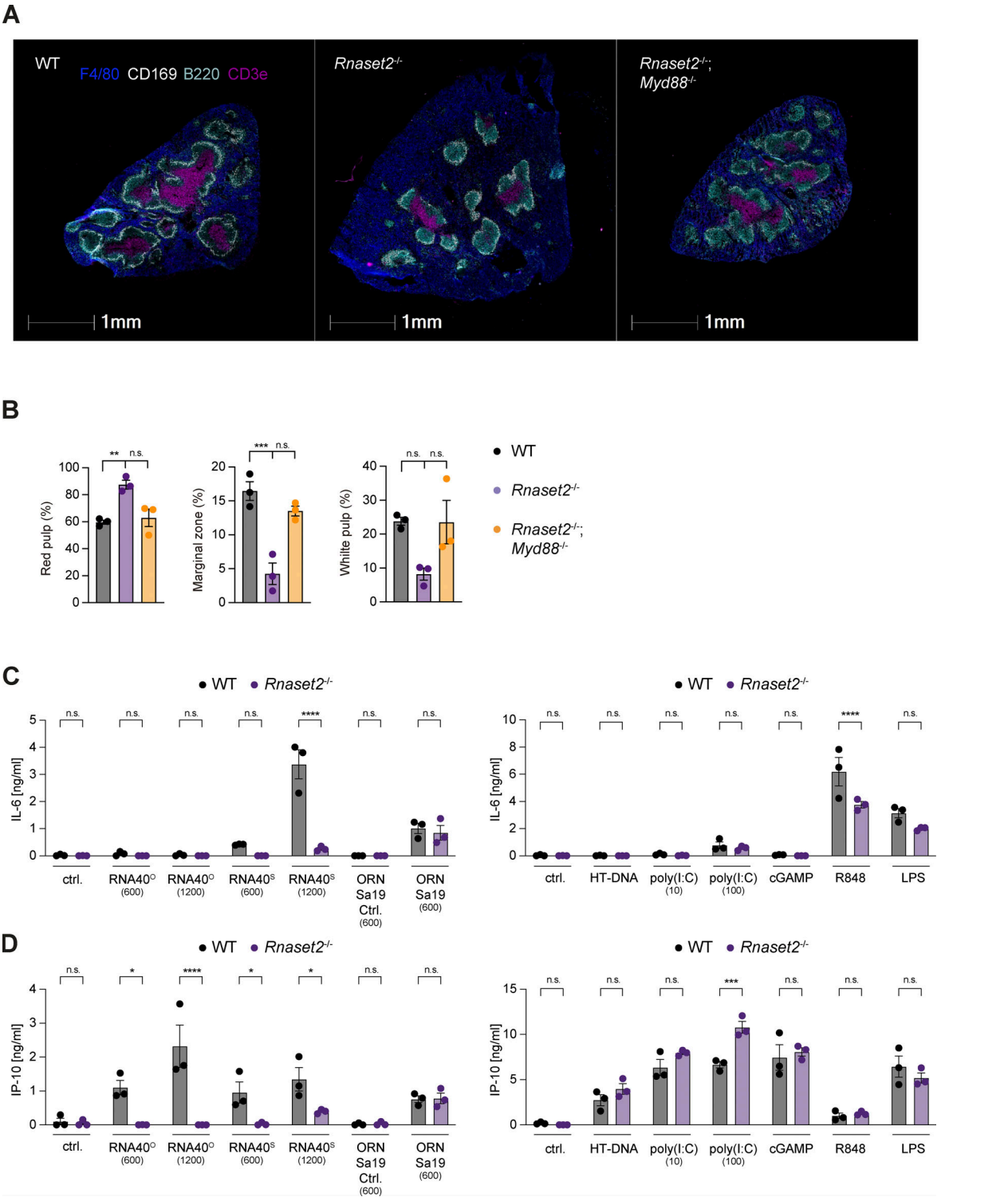

Figure S2. **Spleen architecture of WT and *Rnaset2*$^{-/-}$ mice and cytokine production of PRR-stimulated WT and *Rnaset2*$^{-/-}$ macrophages. (A)** Representative images of F4/80, CD169, B220, and CD3e staining in the spleens of 13-wk-old mice of the indicated genotypes (same samples as in Fig. 2). Scale bars equal 1 mm. **(B)** Quantification of different spleen regions (RP, marginal zone, and white pulp) as a percentage of total spleen area in mice of the indicated genotypes. Data from three mice are presented as mean ± SEM; statistical analysis was conducted using a one-way ANOVA with Dunnett's correction. **(C and D)** BMDMs from WT and *Rnaset2*$^{-/-}$ mice were stimulated with the indicated PRR agonists. RNA oligonucleotide stimuli (left panel) were complexed with poly-L-arginine and used at either 600 or 1,200 ng per transfection. Control stimuli (right panel) were applied as follows: Lipofectamine-transfected herring testes (HT)-DNA (200 ng), poly(I:C) at 10 or 100 µg/ml, cGAMP at 20 µg/ml, R848 at 5 µM, and LPS at 200 ng/ml. Following overnight stimulation, supernatants were collected, and IL-6 (C) or IP-10 (D) production was measured by ELISA. Data from three independent replicates are presented as mean ± SEM; statistical analysis was performed using two-way ANOVA with Šídák's correction. Significance levels are indicated as *P < 0.05, **P < 0.01, ***P < 0.001, and ****P < 0.0001; n.s. = not significant.

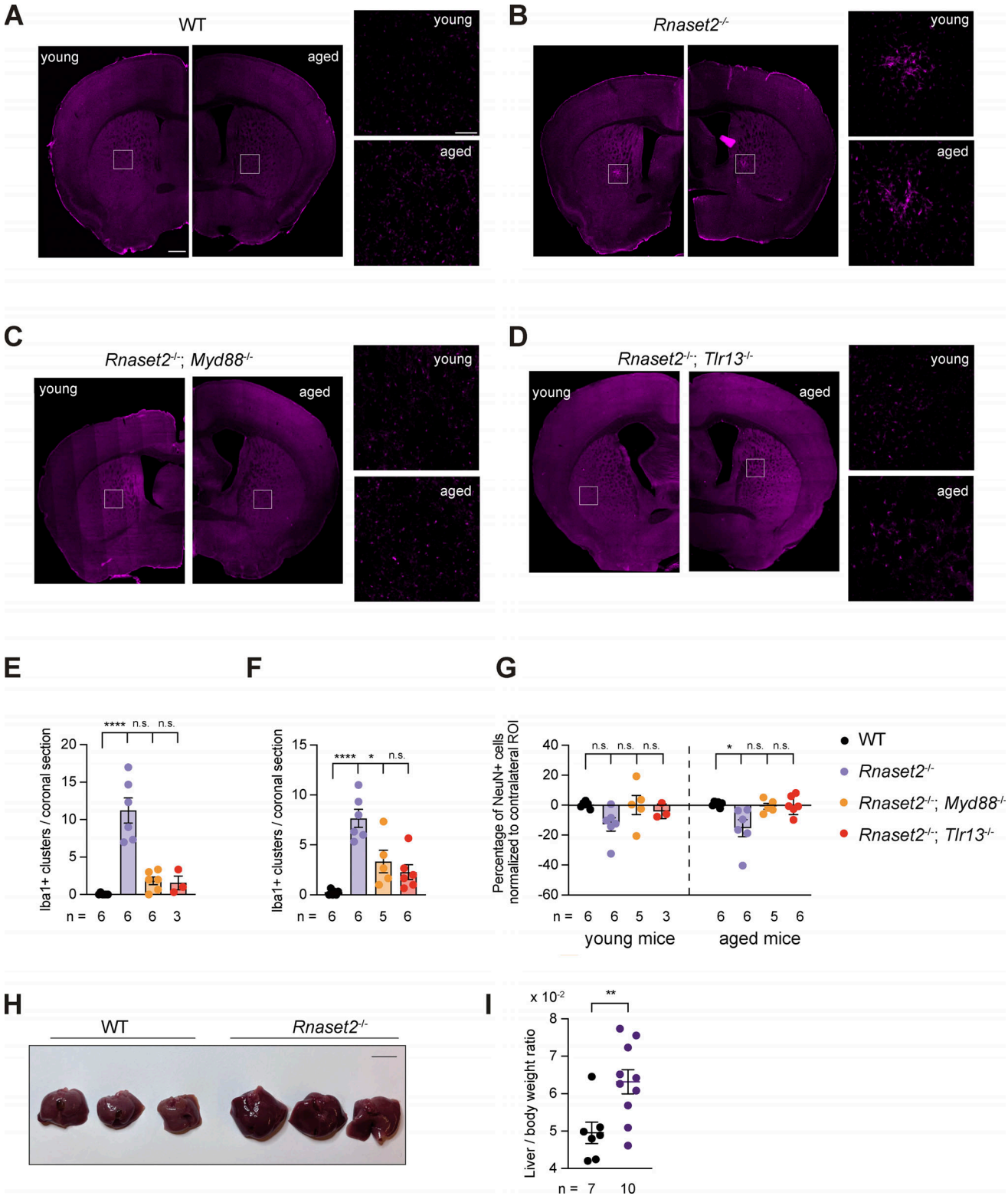

Figure S3. ***Rnaset2*$^{-/-}$ mice present signs of neuroinflammation and *Rnaset2*$^{-/-}$ mice develop hepatomegaly under germ-free conditions. (A–D)** Representative images of Iba1^{+}-stained brain sections from aged mice of the indicated genotypes. Scale bars in the overview images equal 500 µm, scale bars in the insets equal 100 µm. **(E and F)** Number of Iba1^{+} foci in the brains of young (E) and aged (F) mice of the indicated genotypes. **(G)** Percentage of NeuN^{+} cells, normalized to the contralateral ROI, in brain sections from young and aged mice of the indicated genotypes. Data are presented as mean ± SEM; statistical analysis was conducted using a one-way ANOVA with Dunnett's correction. **(H)** Macroscopic appearance of the liver from germ-free 8-wk-old mice of the indicated genotypes. Scale bar equals 1 cm. **(I)** Liver-to-body weight ratio of germ-free 8-wk-old mice from the indicated genotypes. Data are depicted as mean values ± SEM; statistics were calculated using an unpaired two-tailed *t* test. Significance levels are indicated as *P < 0.05, **P < 0.01, and ****P < 0.0001; n.s. = not significant.

Provided online are Table S1 and Table S2. Table S1 shows immune cell populations in young and aged WT and *Rnaset2*$^{-/-}$ mice. Table S2 shows immune cell populations in germ-free WT and *Rnaset2*$^{-/-}$ mice.